A Scalable Active Battery Management System With Embedded Real-Time Electrochemical Impedance Spectroscopy

Eric Din, Christopher Schaef, *Student Member, IEEE*, Keith Moffat, *Student Member, IEEE*, and Jason T. Stauth, *Member, IEEE*

***Abstract*—Electrochemical energy storage is critical for a range of applications spanning electrified transportation and grid energy storage, and there is a need to further improve both the active management and diagnostic capability of current battery management systems. Lithium-based battery chemistries have been favored for their high energy and power densities but require precise management to prevent premature degradation and failure. This work presents an efficient power converter (based on a switched-inductor ladder topology), instrumentation, and an embedded control platform that can provide both active balancing and real-time diagnostic capability through electrochemical impedance spectroscopy (EIS). A digital proportional-integral controller enforces sinusoidal reference signals from a direct digital synthesizer, enabling the power converter to perturb the cells and extract their impedance. Cell-level diagnostics allow for noninvasive measurement of physical electrochemical battery properties that can be used to assess the state of charge and state of health of a battery. A ladder converter prototype was implemented on a printed circuit board to perform EIS on two Panasonic 18650 cells in series. Experimental results showed balancing converter efficiency of 95%, and the accuracy of the prototype was validated through comparison to a state-of-the-art commercial benchtop system.**

***Index Terms*—Battery management, electrochemical impedance spectroscopy (EIS), online diagnostics.**

I. Introduction

ELECTROCHEMICAL energy storage has increased in importance in recent decades due to the rapid growth of electrified transportation and the need to mitigate variability in renewable energy sources [1]. While these applications demand large-scale energy storage, they also require robustness, low cost, and often high energy and power density. Key metrics in most battery systems include state of charge (SOC), which is an estimate of available energy capacity, and state of health (SOH), which is an estimate of remaining useful life [1]–[3]. In addition, many systems and applications desire knowledge of more specific metrics such as series resistance, cell temperature, package strain, presence of gas emission, etc., as these relate to SOH and other specific actions that can be taken in a system controller [4]–[7]. While research into battery state estimation is extensive and often focused on observer-based methods [2], [5]–[10], predominant commercial solutions tend to employ more traditional coulomb counting [11] and very accurate voltage and current measurements and behavioral models using lookup tables and past history [6], [12].

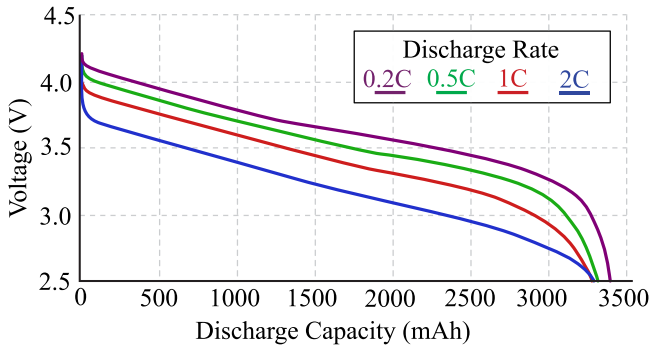

Fig. 1. Discharge characteristics of a Panasonic 18650.

The need for improved battery state and health estimation, as well as diagnostics of specific failure modes, is acute. In many applications, there is a tendency to overdesign the battery pack in terms of capacity, operating range, and charge/discharge rates [4]. Overdesign is compounded by uncertainties in SOC/SOH estimates and the need for long lifetime and high reliability. Uncertainty increases during operation cycles, and conservative limits are placed on the battery as it reaches the end of its capacity. Fig. 1 demonstrates voltage dependencies on SOC and loading conditions that introduce difficulties into state estimation. First, the relatively flat slope of this discharge curve makes it extremely difficult to gain an accurate measurement of SOC from cell voltage alone. Second, the effects of loading conditions can drastically affect the amount of available power in low states of charge as cells are damaged if their voltage drops below 2.5 V. Therefore, accurate state estimation remains a primary issue for battery management systems (BMS) as it directly limits the energy and power density of the battery pack as a whole [5]. For example, coulomb counting works by

Manuscript received March 8, 2016; revised July 11, 2016; accepted August 24, 2016. Date of publication September 8, 2016; date of current version February 27, 2017. Recommended for publication by Associate Editor F. H. Khan.

E. Din, K. Moffat, and J. T. Stauth are with Thayer School of Engineering, Dartmouth, Hanover, NH 03755-8000 USA (e-mail: eric.l.din@gmail.com; keithwmoffat@gmail.com; jason.t.stauth@dartmouth.edu).

C. Schaef was with Thayer School of Engineering, Dartmouth College, Hanover, NH 03755-8000 USA. He is now with the Circuits Research Laboratory, Intel Corporation, Santa Clara, CA 95054-1549 USA (e-mail: christopher.schaef@gmail.com).

Color versions of one or more of the figures in this paper are available online at http://ieeexplore.ieee.org.

Digital Object Identifier 10.1109/TPEL.2016.2607519

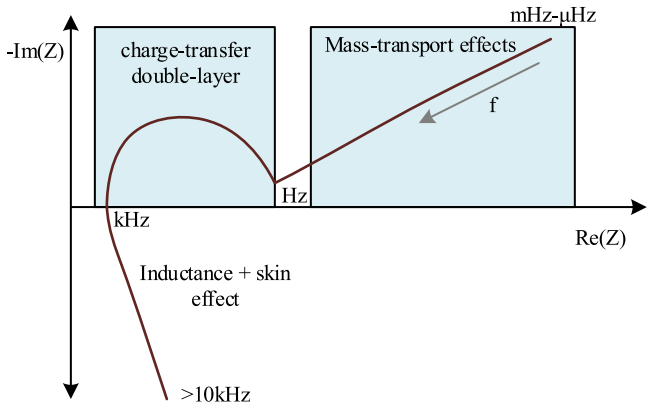

Fig. 2. Representative Nyquist plot for electrochemical cell.

integrating the current into and out of the battery to measure the charge directly. This method does not only require current instrumentation with extremely low offset but also requires knowledge of the current battery capacity of the battery. Often both voltage- and charge-based SOC estimation have to be combined to achieve sufficiently accurate results [13].

Opportunities to implement impedance-based state and health estimation are also well known in the electrochemistry literature [3], [6]–[8], [14], and ongoing electrochemical research aims to establish reliable relationships between impedance data and battery metrics such as SOC, SOH, and internal temperature [15]–[17]. In particular, electrochemical impedance spectroscopy (EIS) is a widely used tool in electrochemical applications as it provides a nondestructive method of analyzing internal processes from external measurements. EIS can characterize specific electrochemical phenomena as they are segmented in the frequency domain in a Nyquist representation, as shown in Fig. 2 [3]. For example, mass-transport effects, the diffusion or migration of ions through the electrolyte, electrodes, or separator can be identified at low frequency (mHz-Hz). Charge transfer in the electrochemical double layer is observed in a regime from hertz to kilohertz. Electromagnetic effects (physical capacitance and inductance) are observed in the kilohertz and higher frequencies [3]. However, the predominant use of EIS is at the benchtop using expensive calibrated galvanostats, potentiostats, or impedance analyzers. Potentiostats and galvanostats have been used for many years in corrosion measurement, coating evaluation, and, more recently, for the characterization of batteries, capacitors, and other energy storage elements [9]. There is significant interest to deploy impedance-based characterization online in large-scale battery arrays [7], [8], [18]. However, this requires a mixture of very accurate instrumentation, actuating capability to perturb the electrochemical operating state, and signal processing to derive the impedance estimate.

Electrochemical management is also made challenging by the fact that large-scale systems are typically constructed of many low-voltage cells configured in parallel and series strings [19]–[24]. Therefore, in most large-scale electrochemical arrays, a BMS is used to monitor and actively regulate (if possible) the states of individual cells or groups of cells in the stack [5], [19], [21], [25], [26]. This helps to reduce uncertainty of SOC and SOH estimates and the possibility to correct minor imbalances among cells or groups of cells, which can lead to differentiated aging profiles and compounded mismatch that can lead to capacity reduction or catastrophic failures within the pack [19].

For certain chemistries, systematic overcharging of series-connected cells will result in equalization without catastrophic damage to cells, albeit on a long time scale [27], [28]. However, active management of lithium-based cell voltages and currents is critical to prevent catastrophic over- or undercharge scenarios, extend lifetime, and maximize capacity [20], [26], [29]. Dissipative cell balancing, in which a resistor or transistor is switched across a cell as it reaches its top-of-charge, has become the predominant solution for its low cost and simplicity. However, this method is only effective during charge cycles and introduces heat generation and power loss [21]. Other methods, based on the utilization of efficient power electronics to transfer charge from cell to cell, build on past work in the field of distributed power electronics [21]–[25], [30]–[33]. These differential power-processing topologies have been proposed and commercially developed [24], [34], but have not gained widespread market adoption. A potential reason may be the relatively high cost compared to the potential benefits. Fig. 3(a) shows dissipative balancing, together with the two more common active balancing topologies based on switching power converters, the ladder converter in Fig. 3(b) and the auxiliary bus converter in Fig. 3(c). Fig. 3 also illustrates how power can be redirected in all three solutions to achieve cell balancing.

Therefore, the challenges of implementing an effective BMS are manifold: the system needs to instrument relevant signals, develop state estimates, monitor for possible failure modes, and (ideally) correct for system asymmetries, mismatch, and imbalance. This work explores a power electronics platform that embeds online EIS on top of a scalable multiple-input multiple-output (MIMO) control algorithm for a distributed array of dc–dc converters. A high-level block diagram of the proposed system is shown in Fig. 4. In the proposed system architecture, small and inexpensive dc–dc converters based on a buck–boost topology configure in a ladder converter as in [25], [26], [35], and [36]. The distributed converter array can shuffle energy in parallel with the battery stack, similar to the partial or differential power processing concept discussed in [24], [31], [32], [35], and [36]. A MIMO control scheme, similar to that developed in [32], is used to regulate individual cell voltages and apply a dynamic perturbation, used for spectroscopic diagnosis.

This work can be compared and positioned relative to the prior art highlighted in Table I. While the past work shown in Table I that implements power electronics all require an external power source or sink (e.g., charger or motor controller) to perform the perturbation [7], [8], [14], [18], [37], this work focuses on the active redistribution of charge already present in the battery pack to generate the EIS perturbation. Also, while majority of past work focuses on EIS applied to a large group of cells, this work targets implementation at the cell level to give highly granular diagnostic information. Many of the past efforts also use exogenous excitation sources (i.e., a motor controller, [7], [18], or battery charger, [8], [14]), which cannot necessarily guarantee uniform perturbation power at all frequencies of interest. In other cases, the perturbation bandwidth is limited (e.g., 100 Hz in [14] and 2 kHz in [7]). Here, we propose to implement

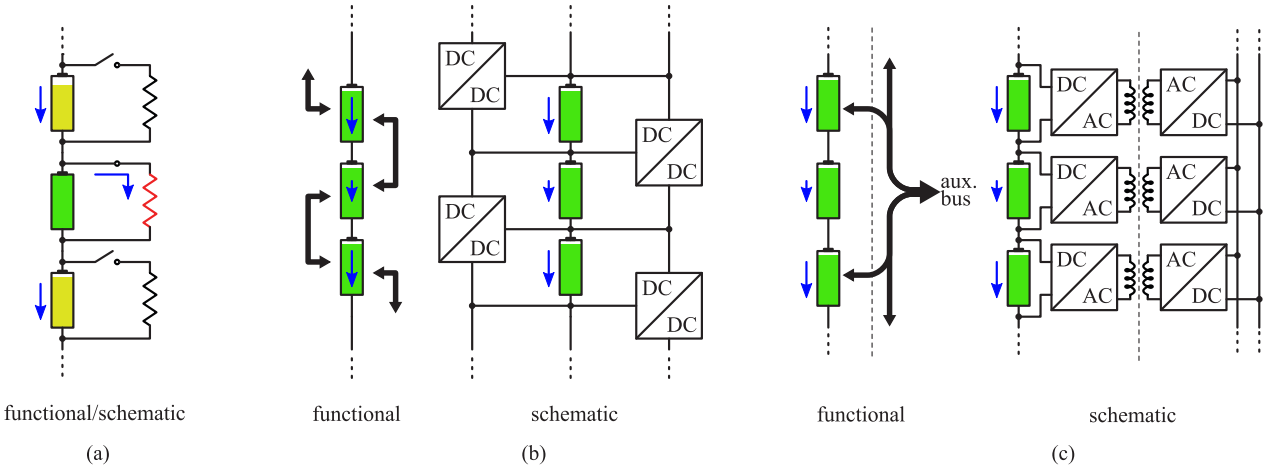

Fig. 3. Dissipative versus charge-transfer balancing. (a) Dissipative balancing. (b) Ladder converter active balancing. (c) Auxiliary bus active balancing.

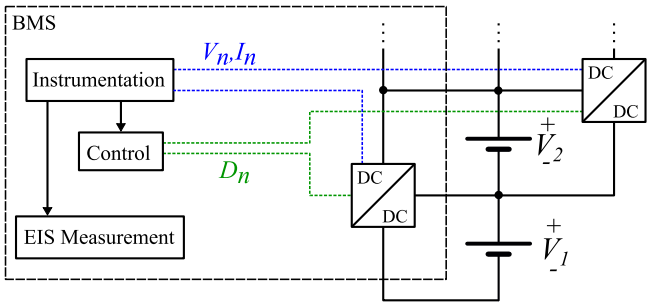

Fig. 4. Proposed BMS for implementation of online spectroscopic diagnostics.

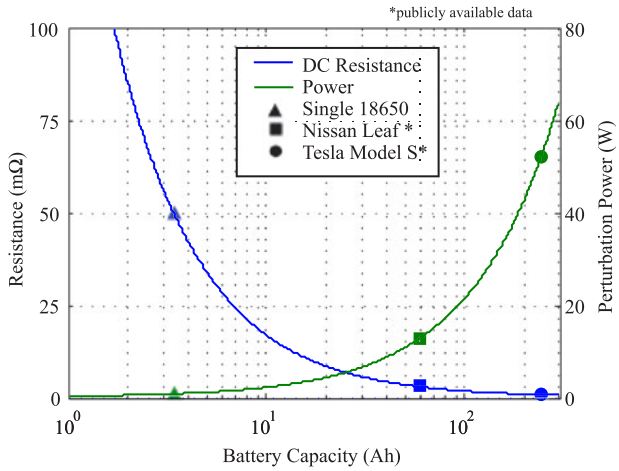

Fig. 5. Impact of cell capacity on EIS power requirements.

a well-regulated dynamical perturbation source and use a novel signal-processing algorithm built in a field-programmable gate array (FPGA) to accurately and rapidly assess spectroscopic characteristics at the cell level in a scalable BMS.

II. Converter Topology and Control

Traditionally, potentiostats or galvanostats use a linear amplifier to enforce a perturbation on a test cell to implement EIS. Because linear amplifiers cannot store any energy, all energy that is required to enforce a sinusoidal perturbation on the battery is eventually dissipated in the linear amplifier. When the potentiostat or galvanostat is plugged into the wall and the cell under test is small, this is hardly an issue. However, this work targets online diagnostics for large battery packs where the use of linear amplifiers becomes impractical.

For a simple demonstration of the limitations of current EIS instruments, consider a single Panasonic 18650 3400-mAh cell with a dc resistance of 50 mΩ. Assuming voltage instrumentation requires a 10-mV perturbation to resolve the impedance of a cell, a perturbation current of 200 mA is required. This results in a peak power of 0.72 W when this current is delivered at the nominal Li-ion voltage of 3.6 V. Assuming dc resistance is inversely proportional to cell capacity, the peak power requirements to enforce a 10-mV perturbation on larger cells become prohibitively large to be enforced with a linear amplifier. Fig. 5 shows the peak required power for a 10-mV perturbation on a single 3.6 V cell of an arbitrary capacity, based on the dc resistance of a single Panasonic 18650 cell. Considering that an electric vehicle battery pack may contain almost a hundred of these cells in series, the hundreds of watts required for the EIS perturbation would quickly lead to heat dissipation issues if implemented in a traditional linear amplifier. Instead, this work leverages efficient power electronics to shuffle energy between battery cells, resulting in an order of magnitude reduction in power loss. Implementing EIS directly in the control of the balancing converter enables the system to actively correct imbalances or problems detected through EIS. For example, consider the proposed alternative where a dc–dc converter supplies the perturbation [the architecture of Fig. 3(b)]. Assuming the converter has 95% efficiency, the total loss is only 2.5% of the total perturbation power. This is because, as the current is recycled as it flows in the stack, at a given point in time, power is only drawn from half of the cells and supplied back to the other half, i.e., every other cell. This provides a significant (40×) reduction of power loss compared to the scenario in Fig. 5.

A. Converter Topology

In this work, we focus on a switched-inductor bidirectional buck–boost converter as the building block of a ladder

TABLE I
OVERVIEW OF PAST WORK, ONLINE EIS

	[7]	[8]	[37]	[18]	[14]	This Work
Cell Level Perturbation	No	No	Yes	No	No	Yes
Test Cell Capacity	2.3 Ah	3 Ah	unavail.	2.6 Ah	unavail.	3.4 Ah
Perturbation Source	Motor Controller	Battery Charger	Linear Amplifier	Load (e.g., motor controller)	Battery Charger	Cell-to-Cell Active Balancer
Perturbation Type	Noise/Multisine	Sawtooth	Sinusoid	Sinusoid	Sinusoid	Sinusoid
Perturbation Current	130 mA (0.06C)	2 A (0.67C)	unavail.	72–750 mA	1 A	160 mA (0.05C)
Perturbation Bandwidth	2 kHz	5 kHz	10 kHz	10 kHz	100 Hz	8 kHz

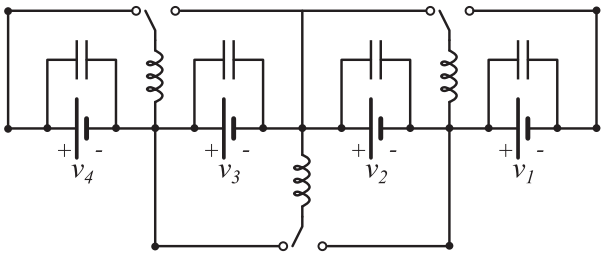

Fig. 6. Switched-inductor ladder converter.

converter that can shuffle power among an arbitrary number of series-connected cells, shown in Fig. 6. A battery stack with N cells in series requires $N-1$ converter stages. In this configuration, each inductor can be placed in parallel with one of the two battery cells, allowing power to be shuffled up and down the series stack. In past efforts, this topology has been applied to battery management and equalization [25] and also for photovoltaic differential power processing [32], [35]. In this work, we use the switched-inductor ladder topology as a candidate architecture for embedded spectroscopic diagnostic capability. However, it should be noted that the techniques presented here could be applied to a wide variety of battery management architectures, e.g., dc-bus topologies [36], auxiliary bus topologies [38], and ladder architectures based on resonant switched capacitor converters [39].

B. Control Scheme

While early battery management circuits were designed to provide nominally fixed 1:1 equalization of series-connected cells, modern chemistries such as Li-ion are extremely sensitive to charge and discharge levels and require accurate regulation. For example, it is known that voltage equalization alone is not sufficient as cell-to-cell variations in impedance can result in different SOC even when cells operate at equal voltages. This has led to a variety of control and regulation schemes, most of which need the ability to adjust cell voltage and current based on an SOC or SOH algorithm. Additionally, leveraging the power converter to implement EIS requires accurate regulation of a sinusoidal signal on the test cell. Fig. 7 shows a high-level block diagram for the implementation of the control scheme.

For the controller design, consider a single stage of the ladder converter, represented in Fig. 8 by switches M_1 and M_2, inductor L, and bypass capacitors C_{b1} and C_{b2}. The converter operates in two phases, where for time D_1T, switch M_1 is closed such that the inductor L is configured in parallel with V_1, and for

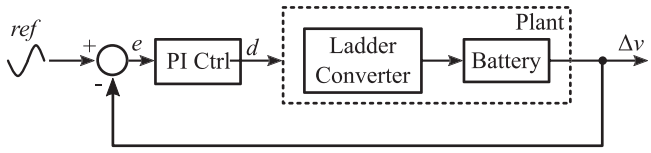

Fig. 7. Control scheme.

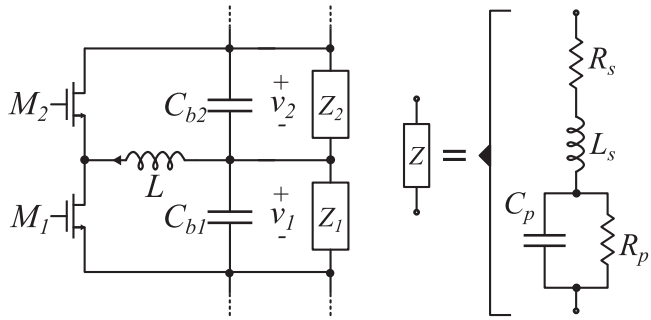

Fig. 8. Single stage of ladder converter for the controller design.

time $(1-D_1)T$, switch M_2 is closed such that the inductor is configured in parallel with V_2. Ignoring parasitics and assuming the average voltage across the inductor is zero, the ratio between V_1 and V_2 in steady state is

$$\frac{V_2}{V_1} = \frac{D_1}{1-D_1}. \tag{1}$$

Therefore, regulation of the voltage ratio between two adjacent cells can be achieved by modulating the duty cycle. However, the voltage ratio in (1) is difficult to instrument and to use as a control parameter as it is nonlinear and computationally intensive. Therefore, as proposed in [32], the control variable is chosen to be Δv, defined as the difference between V_1 and V_2. This provides significant simplification of the control algorithm, since Δv is relatively easy to instrument without computational complexity. In addition, a single duty cycle command, D_i, is mapped directly to a single output, Δv_i, for a given stage of the ladder converter. While a duty-cycle-based controller for the ladder converter in Fig. 6 is inherently a MIMO system, it can be shown that at a nominal 50% duty cycle (in the case assuming cell voltages are approximately equal), the control scheme approximates single-input single-output control [32].

To design a controller capable of enforcing a desired Δv across the frequencies of interest, the converter model in [32] was expanded to include a dynamical battery cell model. As the dominant electrochemical dynamics span a frequency range

TABLE II
COMPONENT VALUES FOR THE CONTROLLER DESIGN

Designator	Value	Unit
L	10	μH
C_{b1}, C_{b2}	2×4.7	μF
R_{s1}, R_{s2}	55	mΩ
L_{s1}, L_{s2}	89	nH
R_{p1}, R_{p2}	20	mΩ
C_{p1}, C_{p2}	860	mF

TABLE III
LINEARIZATION OF THE STATE-SPACE MODEL

Variable	Value	Unit
Duty Cycle D_1	0.5	
Bypass Capacitor $V_{C,b1}, V_{C,b2}$	3.6	V
Inductor i_L	500	mA

from millihertz to kilohertz, a simplified battery cell model, represented in Fig. 8 by R_s, L_s, R_p, and C_p, is used to model the cell impedance in the majority of this frequency range. The model was reduced to the dynamics that are required to analyze controller stability. A more accurate model is presented in Section IV-C. Using this model simplifies controller design while ensuring stability at the converter's corners of operations.

The complete system model, including a single converter stage connected to two battery cell models, was formulated in state space. The state-space model is derived by linearizing the converter equations around a nominal operating point. The linearized model for a single converter stage was derived in [32]. Here, the nominal operating point assumes a balancing current of 250 mA between two cells at equal nominal Li-ion cell voltages, shown in Table III. In addition to the converter model, the battery cell model has to be added, which leads to seven individual energy storage elements: three from the converter and two from each cell. The seventh-order system is represented in state-space form as

$$A = \begin{bmatrix} 0 & 0 & -\frac{\tilde{D}_1}{C_{b1}} & 0 & 0 & -\frac{1}{C_{b1}} & 0 \\ 0 & 0 & \frac{1-\tilde{D}_1}{C_{b2}} & 0 & 0 & 0 & -\frac{1}{C_{b2}} \\ \frac{\tilde{D}_1}{L} & -\frac{1-\tilde{D}_1}{L} & 0 & 0 & 0 & 0 & 0 \\ 0 & 0 & 0 & \frac{-1}{R_{p1}C_{p1}} & 0 & \frac{1}{C_{p1}} & 0 \\ 0 & 0 & 0 & 0 & \frac{-1}{R_{p2}C_{p2}} & 0 & \frac{1}{C_{p2}} \\ \frac{1}{L_{s1}} & 0 & 0 & -\frac{1}{L_{s1}} & 0 & -\frac{R_{s1}}{L_{s1}} & 0 \\ 0 & \frac{1}{L_{s2}} & 0 & 0 & -\frac{1}{L_{s2}} & 0 & -\frac{R_{s2}}{L_{s2}} \end{bmatrix}$$

$$B = \begin{bmatrix} -\frac{\tilde{I}_L}{C_b} & -\frac{\tilde{I}_L}{C_b} & \frac{\tilde{V}_1 + \tilde{V}_2}{L} & 0 & 0 & 0 & 0 \end{bmatrix}^T$$

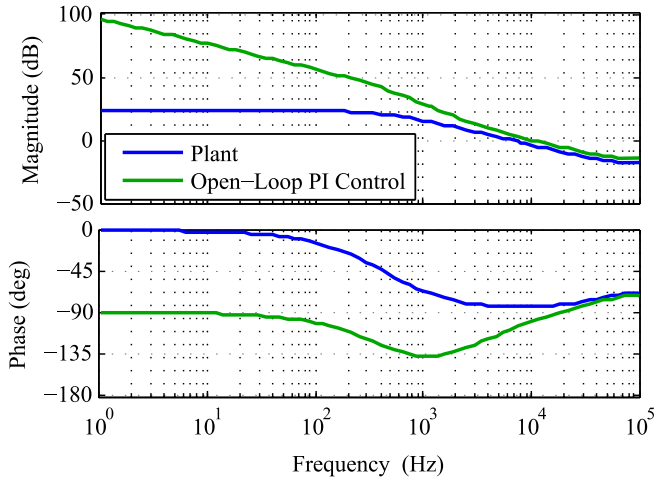

Fig. 9. Bode plot of the state-space modeled system, showing PI controller.

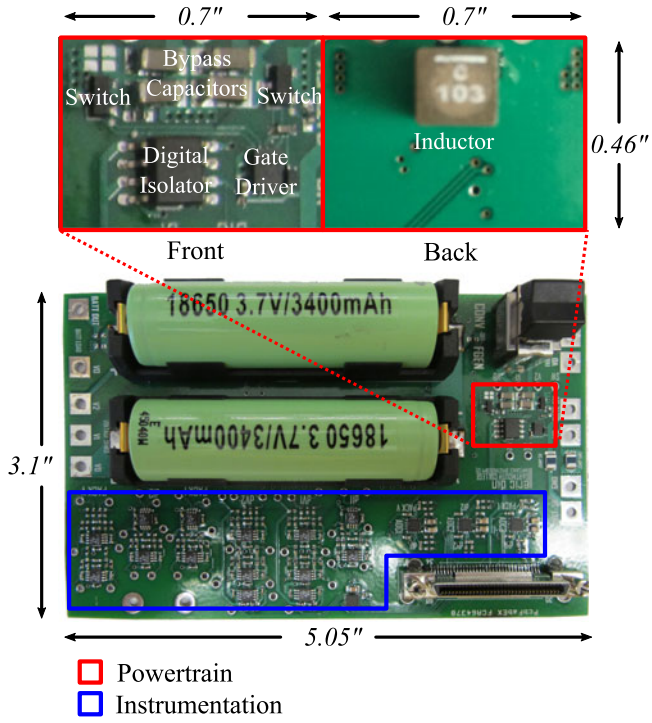

Fig. 10. Prototype PCB.

$$C = \begin{bmatrix} -1 & 1 & 0 & 0 & 0 & 0 & 0 \end{bmatrix}$$
$$D = 0$$
$$x = \begin{bmatrix} V_1 & V_2 & I_L & V_{Cp1} & V_{Cp2} & I_{Ls1} & I_{Ls2} \end{bmatrix}^T$$
$$u = d_1, \qquad y = \Delta v.$$

Table II provides component values for the schematic in Fig. 8. A proportional-integral (PI) controller was chosen to provide the desired frequency response, shown in Fig. 9. The integral control term provides low steady-state error at low frequencies for balancing scenarios. However, due to a low frequency pole in the tens of Hertz range from the parallel *RC* in the battery cell model, integral control alone would cause

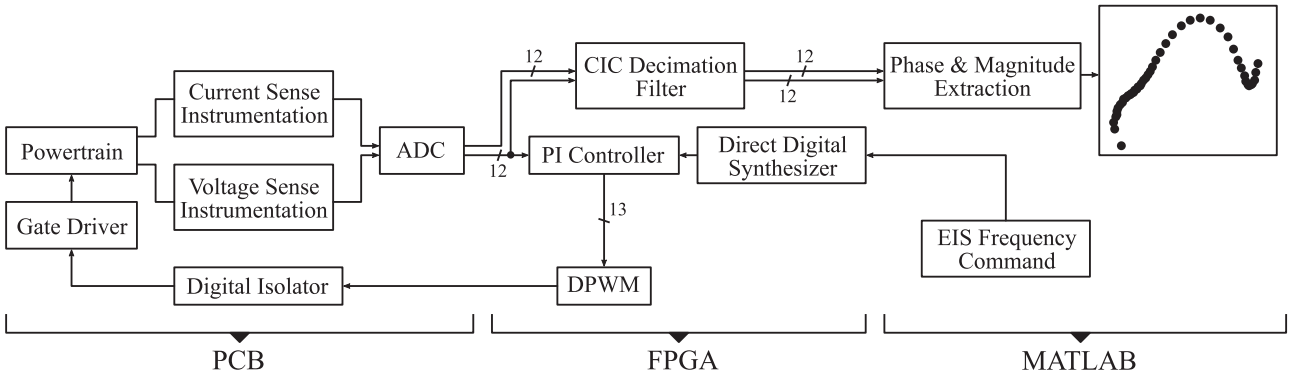

Fig. 11. System diagram of EIS implementation.

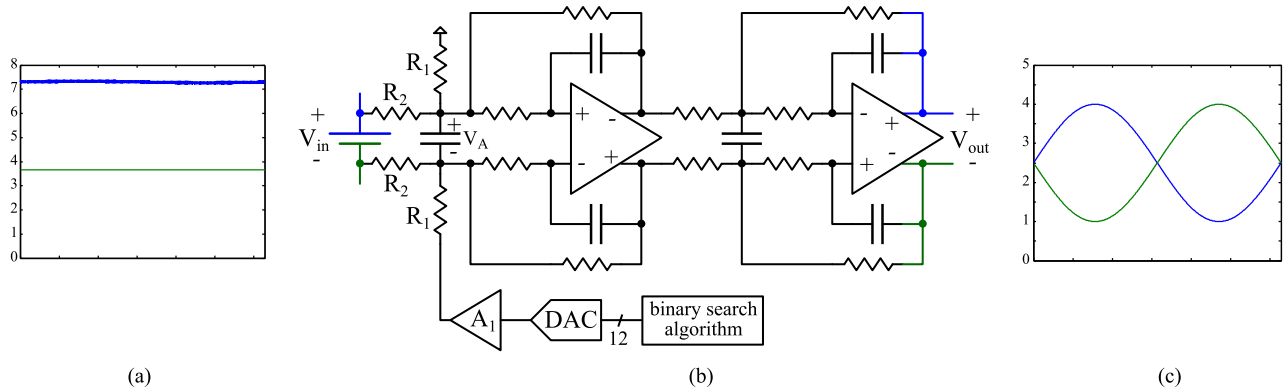

Fig. 12. (a) Battery cell voltage is measured through a (b) dc servo-loop circuit to remove both the dc offset and OCV of a battery cell before the (c) filtered output is digitized by the ADC.

instability resulting from insufficient phase margin. Therefore, a proportional control term was added to place a zero to maintain a conservative phase margin of 80°, resulting in a control bandwidth of 10 kHz, which is sufficiently fast to capture the battery dynamics of interest. The above conditions and constraints give continuous-time controller gains of $k_p = 1.495$ and $k_i = 27.706$.

III. Implementation

This section describes the implementation of EIS in the ladder converter. A single stage of the ladder converter, two battery holders, and voltage and current instrumentation was implemented on a 3.1 in × 5.05 in four-layer printed circuit board (PCB), seen in Fig. 10. The single stage of the ladder converter, consisting of a Coilcraft XAL5050-103 10-μH inductor, 4 × 4.7-μF ceramic bypass capacitors, power switches, a synchronous gate driver, and a digital isolator, occupies 0.32 in^2 of board area. A Digilent Genesys FPGA board is used for analog-to-digital converter (ADC) data filtering, digital pulse width modulation (DPWM) generation, and control implementation. The signal chain for measuring battery cell impedance is illustrated in Fig. 11.

A. Perturbation Generation

A direct digital synthesizer (DDS) was implemented on the FPGA to generate arbitrary sinusoidal reference signals with frequency resolution of 1.5 mHz. With the converter operating in a nominal balancing mode (typically $\Delta\bar{v} = 0V$), the DDS creates a sinusoidal perturbation from a magnitude and frequency command. The feedback controller then enforces this signal on the cell. The duty cycle is produced from a 9-bit DPWM with 4 bits of dithering operating at a switching frequency of 880 kHz.

B. Instrumentation

Cell impedance is calculated from the magnitude and phase relationship between the current and voltage of a battery cell. Therefore, accurate and fast sampling of cell voltage and current is necessary for a reliable impedance measurement. Voltage and current values are digitized through TI ADS7254 12-bit ADCs for each individual cell as well as the two-cell stack. Each voltage and current is measured through its own dedicated ADC channel driven by shared triggers and serial clocks to ensure the measurements are synchronous and do not introduce a phase error.

1) Voltage Sense: A typical lithium-based cell's open circuit voltage (OCV) ranges from 2.5 to 4.2 V depending on SOC, while a typical EIS perturbation has an amplitude of 10 mV. Digitizing the entire voltage range of a lithium-based cell would provide insufficient resolution to accurately measure the response of the cell to a small perturbation. Therefore, the dc component of the cell voltage must be removed to take advantage of the full-scale range of the ADC. Unfortunately, dynamics

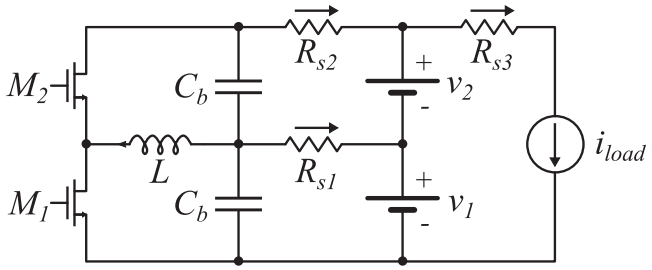

Fig. 13. Balancing current-sensing scheme.

of interest in the low-frequency range (single digit millihertz) prevent the use of a simple ac-coupling capacitor. Instead, a digital servo-loop was implemented to remove the dc component of the cell voltage, effectively high-pass filtering and amplifying only the ac perturbation. Fig. 12(b) shows the circuit used to implement the dc servo-loop. To accommodate battery cells that may be above the supply voltage of the instrumentation, the voltage across each cell is divided by the resistive divider consisting of R_1 and R_2:

$$V_{A+} = V_{\text{in}+}\frac{R_1}{R_1+R_2} \tag{2}$$

$$V_{A-} = \frac{A_1 V_{\text{DAC}} R_2 + V_{\text{in}-} R_1}{R_1+R_2} \tag{3}$$

where $V_{\text{in}+}$ and $V_{\text{in}-}$ are the positive and negative terminals of the battery whose voltage is being measured, and V_{A+} and V_{A-} are the divided battery voltages, as indicated in Fig. 12. A binary search algorithm adjusts the output of the DAC so that the differential output of the servo-loop is 0 V, matching V_{DAC} to the cell voltage, V_{in}. The gain stage A_1 is included to utilize the full-scale range of the DAC to match the cell voltage without loss of resolution. Equating (2) and (3) removes the dc component of V_A and gives the target value of A_1 as R_1/R_2. Two fully differential gain stages are used to provide a gain of 24.5 V/V. Each stage also forms a second-order Butterworth low-pass filter with a cutoff frequency of 100 kHz. Combined with the voltage divider gain of $\frac{1}{6}$, the overall gain of the circuit is 100 V/V with a fourth-order active filter with a cutoff frequency of 100 kHz.

Fig. 12(a) shows the input to the circuit as some small ac perturbation on a cell's OCV. The circuit in Fig. 12(b) removes both the OCV of the cell and the common mode resulting from the cell not being connected to ground. Fig. 12(c) shows the fully differential output of the last stage of the amplifier with only the ac component of the cell voltage amplified. Digitization through the 5-V 12-bit ADC gives a voltage sense resolution of 24.4 μV.

2) Current Sense: While individual cell voltage measurement is a common BMS feature, individual cell current measurement presents a challenge in traditional BMS architectures. As battery load currents can be in the hundreds of Amperes, inserting a current sense resistor in series with each cell is not practical as it would result in large power losses. However, with the proposed ladder converter, cell current can be estimated by measuring only the balancing currents in each stage of the converter as shown in Fig. 13. A simple current balance at each cell node can be performed to extract the absolute current into and out of each cell:

$$i_2 = i_{\text{Rs},2} - i_{\text{load}} \tag{4}$$

$$i_1 = i_2 + i_{\text{Rs},1} = i_{\text{Rs},1} + i_{\text{Rs},2} - i_{\text{load}}. \tag{5}$$

where i_1 and i_2 are the currents through cell 1 and 2, and $i_{\text{Rs},1}$ and $i_{\text{Rs},2}$ are the currents through sense resistors R_{s1} and R_{s2}, respectively. Assuming that the total current out of the series stack of cells, i_{load}, is constant relative to the EIS perturbation frequency, then each cell's impedance can be calculated using only the balancing currents measured with each current

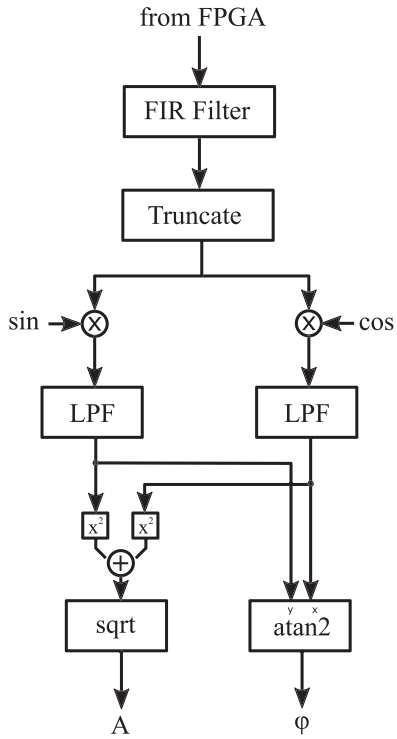

Fig. 14. Filtering and I/Q demodulator signal train.

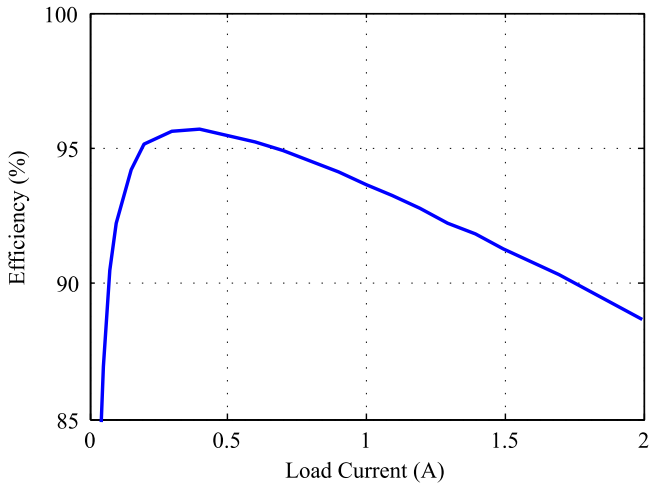

Fig. 15. Converter efficiency measured in 2:1 mode.

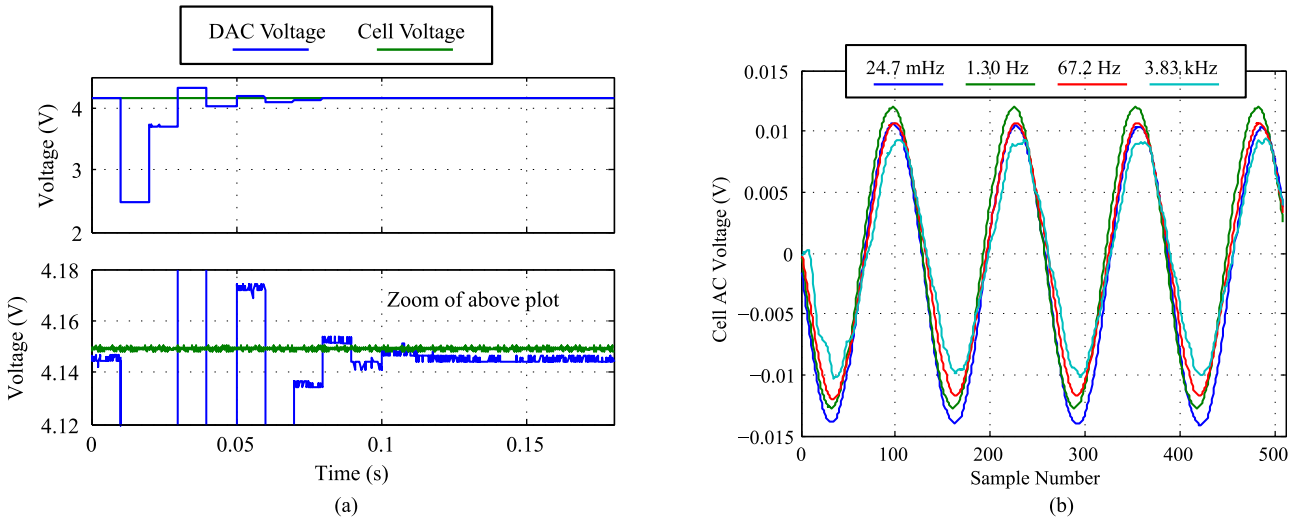

Fig. 16. Voltage instrumentation verification. (a) Binary search to set DAC voltage to cell OCV. (b) Digitized output of CIC filter across multiple frequency decades.

sense resistor R_s. This current-sensing method is scalable to an arbitrary number of series-connected cells without adding additional current sense resistors in series with the stack of cells. On the prototype circuit board, current is measured across a 20-mΩ current sense resistor, amplified through a current sense amplifier with a gain of 50 V/V, and filtered through a second-order Butterworth low-pass active filter with a cutoff frequency of 100 kHz and a gain of 2 V/V. Digitization through the 5-V 12-bit ADC gives a current sense resolution of 1.2 mA.

C. Impedance Calculation

Voltage and current data from each ADC passes through a variable-downsample cascaded integrator-comb (CIC) decimation filter whose downsample rate is determined by the frequency of the perturbation. Thus, the timescale of perturbation of an arbitrary frequency is normalized to a fixed number of samples per period, enabling the same postprocessor to extract the impedance for all frequencies. Both current and voltage signals pass through the same digital signal-processing chain, which ensures that any phase contributions do not affect the impedance calculation. Data from a specified number of periods are stored on FPGA RAM and then collected and compiled for postprocessing. This process is repeated for a range of frequencies. After data collection has completed, the current and voltage data for each cell are filtered by an finite impulse response (FIR) filter, truncated to minimize the effects of startup transients, and processed by an I/Q demodulator to extract the magnitude and phase relationship. This process is detailed in Fig. 14. The impedance is then plotted on an inverted reactance versus resistance plot (Nyquist plot), shown in Section IV in Figs. 17 and 18.

IV. Experimental Results

A. System Verification

1) Powertrain: The performance of the single ladder converter stage was evaluated with the converter operating open loop with a 50% duty cycle. Since cell voltages in a string are always approximately equal, the converter will mostly operate close to 50% duty cycle. As seen in Fig. 15, peak efficiency was measured at 95.7% at 400-mA load current, which is the approximate range of the peak balancing currents required in this application. However, it can be appreciated that the efficiency profile of the converter (and the converter itself) could easily be tuned or designed to fit the specification of different applications. While there are a range of opportunities to improve the converter design (e.g., implement light-load high-efficiency modes), that is not the focus here.

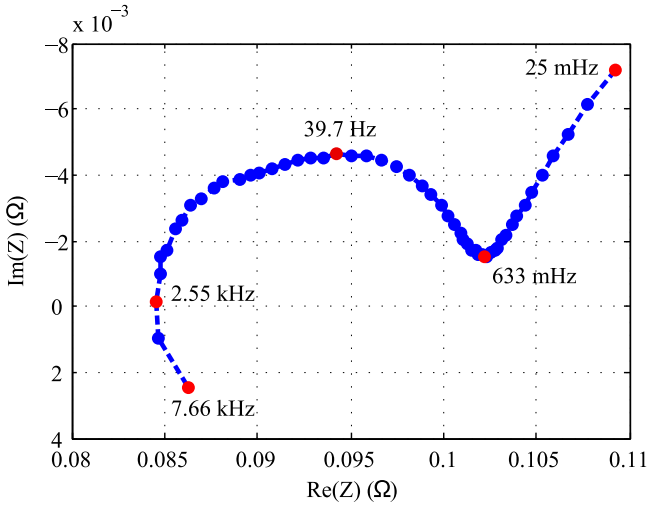

Fig. 17. Example Nyquist plot of a Panasonic 18650 3400-mAh cell at OCV voltage of 3.65 V.

2) Instrumentation: Fig. 16 shows how the dc component of the cell's OCV is largely removed through the implementation of a digital servo loop. Fig. 16(a) shows the binary search algothrim used to set the DAC voltage to the OCV of the cell. In this manner, the dc voltage of the cell is largely removed and only the ac component of the cell voltage is digitized and filtered through

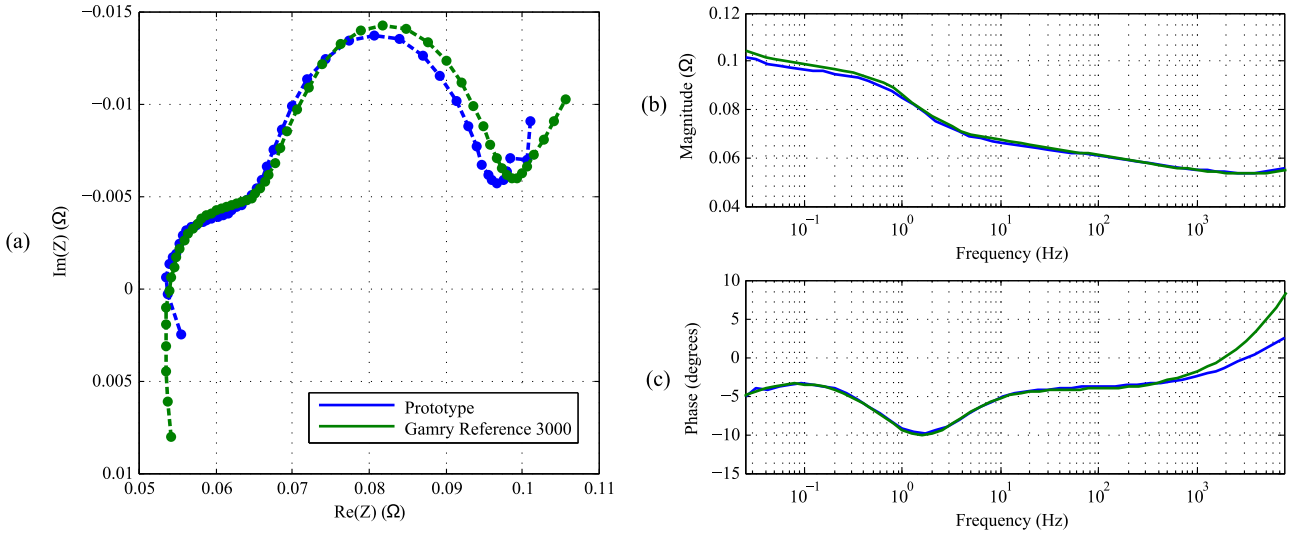

Fig. 18. Comparison of protoype to the Gamry Reference 3000 potentiostat.

the CIC filter. The output of the CIC filter for perturbations of multiple frequencies is plotted in Fig. 16(b), demonstrating the effective removal of most of the dc component of cell voltage.

3) Impedance Calculation: The method described above to calculate impedance from current and voltage data was verified on two Panasonic 18650 3400-mAh Li-ion battery cells. Fig. 17 shows the Nyquist plot of impedance measurements of one 18650 cell at nominal voltage of 3.65 V at perturbation frequencies ranging from 25 mHz to 7.66 kHz. Features of the impedance spectrum such as the low-frequency tail and negative reactance semicircle are consistent with the representative Nyquist plot shown in Fig. 2.

B. Verification Against State of the Art

The prototype in this work was compared to one commercially available potentiostat, the Gamry Reference 3000. The Gamry is an industry standard electrochemical characterization instrument capable of highly accurate EIS measurements. The prototype system ran 47 perturbations ranging from 25 mHz to 7.66 kHz on a pair of Panasonic 18650 cells, and the Gamry ran 57 perturbations ranging from 20 mHz to 8.02 kHz on one of the same cells. Fig. 18 shows the comparison of the two system's impedance measurements. In Fig. 18(a), it can be seen that the prototype system is capable of producing impedance data that is in good agreement with the reference measurement. The magnitude and phase plots in Fig. 18(b) and (c) give a little more insight into the Nyquist plot discrepancies between the two systems. At low frequencies, there is a maximum of 3% magnitude discrepancy that decreases with increasing frequency. At frequencies above 1 kHz, there is an increasing phase discrepancy between the two systems. The frequency at which the Nyquist plot crosses the real axis from negative to positive reactance marks the frequency at which inductance begins to dominate. Battery cell impedance models may include series inductance to represent inductance from current collectors and cabling, e.g., a value of 170 nH in [40]. Despite efforts to twist wires and minimize the inductance of the Gamry setup, the relatively long leads to the free-hanging battery holder resulted in an *LCR*-meter measurement in the hundreds of nanohenry. Therefore, the phase discrepancy in frequencies above the real axis crossing can be largely attributed to the added inductance from the Gamry's measurement setup compared to the board-mounted battery holders used in the prototype.

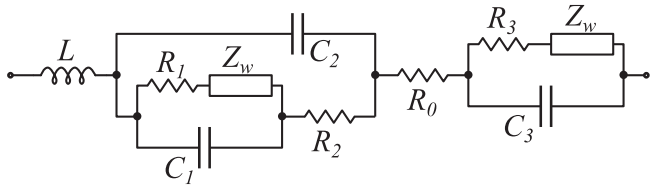

Fig. 19. Full battery cell impedance model, modified from [40].

C. Circuit Equivalent Model

Online applications introduce data storage constraints, making it impractical to store entire sets of EIS data. Therefore, online applications require mapping the EIS data to battery cell impedance circuit equivalent models [41]. The battery cell model in [40] was developed to reflect electrical equivalents of physical electrochemical processes, enabling the tracked parameters to be used as a metric of the state of physical processes within the battery. This work uses a simplified version of the impedance model developed in [40] and is shown in Fig. 19. The main difference between the model in [40] and this work is that the Faradaic impedance described in [40], used to capture charge-transfer resistance and solid-phase diffusion impedance, is replaced with an explicit resistor and the Warburg element taken from the Randles model, defined as $Z_w = A_w/\sqrt{j\omega}$.

A least-squares regression analysis was performed to find component values for the battery cell impedance model such that the modeled impedance optimally matches the measured impedance of a test cell. The regression used a Levenberg–Marquardt regression on only the imaginary impedance to

TABLE IV
VALUES OF COMPONENTS IN THE BATTERY CELL IMPEDANCE MODEL

Designator	Value	Unit
L	150	nH
R_0	61.3	mΩ
R_1	4.4	mΩ
C_1	2.94	F
R_2	5.2	mΩ
C_2	624	mF
R_3	37.6	mΩ
C_3	21.4	F
A_w	850	$\mu\Omega/\sqrt{s}$

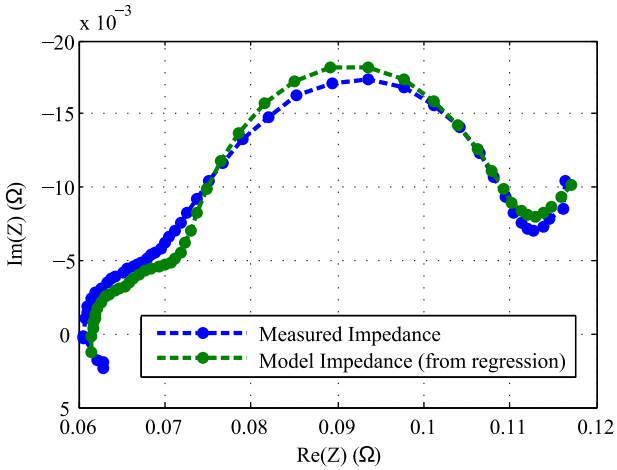

Fig. 20. Curve-fitting regression for Panasonic 18650 at top of charge.

minimize percentage error across the entire frequency spectrum. Table IV contains the component values for the battery cell impedance model shown in Fig. 19. Fig. 20 shows a Nyquist plot comparison of the measured and modeled impedance of a cell at top of charge. Some discrepancies between the measured and modeled impedances remain, e.g., the two semicircular regions of the modeled impedance are more distinct than that of the measured impedance. Still, the regression is capable of reasonable matching, and storing component values for a battery cell model instead of data for an entire range of frequencies could be used as a way to track the state of internal processes of the battery in an online application.

V. CONCLUSION

This work presented a method for implementing EIS in an efficient active-balancing BMS. In addition to effective and efficient cell balancing, it was shown that an appropriate control scheme can enforce a sinusoidal perturbation on a battery cell. Proper instrumentation to measure the cell's response to an external voltage perturbation enables the noninvasive extraction of the condition of internal electrochemical processes through industry-standard EIS. Validation of the prototype BMS against a commercially available benchtop potentiostat confirmed the accuracy of battery cell impedance measurements. Finally, a method for fitting a battery impedance model to test data was presented to track the state of internal electrochemical processes.

REFERENCES

[1] J. B. Goodenough, H. D. Abruna, and M. V. Buchanan, "Basic Research Needs for Electrical Energy Storage. Report of the Basic Energy Sciences Workshop on Electrical Energy Storage, April 2-4, 2007," USDOE Office of Science, Washington, DC, USA, Apr. 2007. [Online]. Available: http://www.osti.gov/servlets/purl/935429-ERrVsI/

[2] G. L. Plett, "Sigma-point Kalman filtering for battery management systems of LiPB-based HEV battery packs. Part 1: Introduction and state estimation," *J. Power Sources*, vol. 161, no. 2, pp. 1356–1368, 2006.

[3] A. Jossen, "Fundamentals of battery dynamics," *J. Power Sources*, vol. 154, no. 2, pp. 530–538, 2006.

[4] D. Doughty, and E. P. Roth, "A general discussion of Li ion battery safety," *Electrochem. Soc. Interface*, vol. 21, no. 2, pp. 37–44, 2012.

[5] L. Lu, X. Han, J. Li, J. Hua, and M. Ouyang, "A review on the key issues for lithium-ion battery management in electric vehicles," *J. Power Sources*, vol. 226, pp. 272–288, Mar. 2013. [Online]. Available: http://linkinghub.elsevier.com/retrieve/pii/S0378775312016163

[6] J. Remmlinger, M. Buchholz, M. Meiler, P. Bernreuter, and K. Dietmayer, "State-of-health monitoring of lithium-ion batteries in electric vehicles by on-board internal resistance estimation," *J. Power Sources*, vol. 196, no. 12, pp. 5357–5363, Jun. 2011. [Online]. Available: http://linkinghub.elsevier.com/retrieve/pii/S0378775310013534

[7] D. A. Howey, P. D. Mitcheson, V. Yufit, G. J. Offer, and N. P. Brandon, "Online measurement of battery impedance using motor controller excitation," *IEEE Trans. Veh. Technol.*, vol. 63, no. 6, pp. 2557–2566, Jul. 2014.

[8] R. Koch, R. Kuhn, I. Zilberman, and A. Jossen, "Electrochemical impedance spectroscopy for online battery monitoring—Power electronics control," in *Proc. 2014 16th Eur. Conf. Power Electron. Appl.*, 2014, pp. 1–10.

[9] S. Buller, M. Thele, R. W. A. A. De Doncker, and E. Karden, "Impedance-based simulation models of supercapacitors and li-ion batteries for power electronic applications," *IEEE Trans. Ind. Appl.*, vol. 41, no. 3, pp. 742–747, May/Jun. 2005.

[10] D. Vinh Do, C. Forgez, K. El Kadri Benkara, and G. Friedrich, "Impedance observer for a Li-ion battery using Kalman filter," *IEEE Trans. Veh. Technol.*, vol. 58, no. 8, pp. 3930–3937, Oct. 2009. [Online]. Available: http://ieeexplore.ieee.org/lpdocs/epic03/wrapper.htm?arnumber=5184857

[11] K. S. Ng, C.-S. Moo, Y.-P. Chen, and Y.-C. Hsieh, "Enhanced coulomb counting method for estimating state-of-charge and state-of-health of lithium-ion batteries," *Appl. Energy*, vol. 86, no. 9, pp. 1506–1511, Sep. 2009. [Online]. Available: http://linkinghub.elsevier.com/retrieve/pii/S0306261908003061

[12] M. Einhorn, F. V. Conte, C. Kral, and J. Fleig, "Comparison, selection, and parameterization of electrical battery models for automotive applications," *IEEE Trans. Power Electron.*, vol. 28, no. 3, pp. 1429–1437, Mar. 2013. [Online]. Available: http://ieeexplore.ieee.org/lpdocs/epic03/wrapper.htm?arnumber=6252063

[13] K. W. E. Cheng, B. P. Divakar, H. Wu, K. Ding, and H. F. Ho, "Battery-management system (BMS) and SOC development for electrical vehicles," *IEEE Trans. Veh. Technol.*, vol. 60, no. 1, pp. 76–88, Jan. 2011. [Online]. Available: http://ieeexplore.ieee.org/lpdocs/epic03/wrapper.htm?arnumber=5609223

[14] Y.-D. Lee, S.-Y. Park, and S.-B. Han, "Online embedded impedance measurement using high-power battery charger," *IEEE Trans. Ind. Appl.*, vol. 51, no. 1, pp. 498–508, Jan. 2015. [Online]. Available: http://ieeexplore.ieee.org/lpdocs/epic03/wrapper.htm?arnumber=6856173

[15] A. Zenati, P. Desprez, and H. Razik, "Estimation of the SOC and the SOH of Li-ion batteries, by combining impedance measurements with the fuzzy logic inference," in *Proc. 36th Annu. Conf. IEEE Ind. Electron. Soc.*, Nov. 2010, pp. 1773–1778. [Online]. Available: http://ieeexplore.ieee.org/lpdocs/epic03/wrapper.htm?arnumber=5675408

[16] W. Waag, S. Käbitz, and D. U. Sauer, "Experimental investigation of the lithium-ion battery impedance characteristic at various conditions and aging states and its influence on the application," *Appl. Energy*, vol. 102, pp. 885–897, Feb. 2013. [Online]. Available: http://linkinghub.elsevier.com/retrieve/pii/S030626191200671X

[17] J. Zhu, Z. Sun, X. Wei, and H. Dai, "A new lithium-ion battery internal temperature on-line estimate method based on electrochemical impedance spectroscopy measurement," *J. Power Sources*, vol. 274, pp. 990–1004, Jan. 2015. [Online]. Available: http://linkinghub.elsevier.com/retrieve/pii/S0378775314018011

[18] W. Huang and J. A. Qahouq, "An online battery impedance measurement method using DC-DC power converter control," *IEEE Trans. Ind. Electron.*, vol. 61, no. 11, pp. 5987–5995, Nov. 2014. [Online]. Available: http://ieeexplore.ieee.org/lpdocs/epic03/wrapper.htm?arnumber=6766212

[19] J. Cao, N. Schofield, and A. Emadi, "Battery balancing methods: A comprehensive review," in *Proc. IEEE Veh. Power Propulsion Conf.*, 2008, pp. 1–6.
[20] W. C. Lee, D. Drury, and P. Mellor, "Comparison of passive cell balancing and active cell balancing for automotive batteries," in *Proc. 2011 IEEE Veh. Power Propulsion Conf.*, 2011, pp. 1–7.
[21] J. W. Kimball, B. T. Kuhn, and P. T. Krein, "Increased performance of battery packs by active equalization," in *Proc. IEEE Veh. Power Propulsion Conf.*, Sep. 2007, pp. 323–327.
[22] D. Costinett *et al.*, "Active balancing system for electric vehicles with incorporated low voltage bus," in *Proc. 2014 IEEE Appl. Power Electron. Conf. Expo.*, Mar. 2014, pp. 3230–3236. [Online]. Available: http://ieeexplore.ieee.org/lpdocs/epic03/wrapper.htm?arnumber=6803768
[23] M. M. U. Rehman, F. Zhang, M. Evzelman, R. Zane, and D. Maksimovic, "Control of a series-input, parallel-output cell balancing system for electric vehicle battery packs," in *Proc. 2015 IEEE 16th Workshop Control Modeling Power Electron.*, Jul. 2015, pp. 1–7. [Online]. Available: http://ieeexplore.ieee.org/lpdocs/epic03/wrapper.htm?arnumber=7236506
[24] C. Pascual and P. Krein, "Switched capacitor system for automatic series battery equalization," in *Proc. 12th Annu. Appl. Power Electron. Conf. Expo.*, 1997, vol. 2, pp. 848–854.
[25] N. H. Kutkut and D. M. Divan, "Dynamic equalization techniques for series battery stacks," in *Proc. 18th Int. Telecommun. Energy Conf.*, 1996, pp. 514–521.
[26] M. Einhorn, W. Roessler, and J. Fleig, "Improved performance of serially connected Li-ion batteries with active cell balancing in electric vehicles," *IEEE Trans. Veh. Technol.*, vol. 60, no. 6, pp. 2448–2457, Jul. 2011.
[27] P. Krein and R. Balog, "Life extension through charge equalization of lead-acid batteries," in *Proc. 24th Annu. Int. Telecommun. Energy Conf.*, 2002, pp. 516–523. [Online]. Available: http://ieeexplore.ieee.org/lpdocs/epic03/wrapper.htm?arnumber=1048705
[28] A. Lohner, E. Karden, and R. de Doncker, "Charge equalizing and lifetime increasing with a new charging method for VRLA batteries," in *Proc. Power Energy Syst. Converging Markets*, 1997, pp. 407–411. [Online]. Available: http://ieeexplore.ieee.org/lpdocs/epic03/wrapper.htm?arnumber=645919
[29] A. Khaligh and Z. Li, "Battery, ultracapacitor, fuel cell, and hybrid energy storage systems for electric, hybrid electric, fuel cell, and plug-in hybrid electric vehicles: State of the art," *IEEE Trans. Veh. Technol.*, vol. 59, no. 6, pp. 2806–2814, Jul. 2010. [Online]. Available: http://ieeexplore.ieee.org/lpdocs/epic03/wrapper.htm?arnumber=5446335
[30] S. Rajapandian, K. Shepard, P. Hazucha, and T. Karnik, "High-voltage power delivery through charge recycling," *IEEE J. Solid-State Circuits*, vol. 41, no. 6, pp. 1400–1410, Jun. 2006.
[31] P. S. Shenoy, B. B. Johnson, and P. T. Krein, "Differential power processing architecture for increased energy production and reliability of photovoltaic systems," in *Proc. IEEE Appl. Power Electron. Conf.*, Feb. 2012, pp. 1987–1994.
[32] C. Schaef and J. T. Stauth, "Multilevel power point tracking for partial power processing photovoltaic converters," *IEEE J. Emerg. Sel. Topics Power Electron.*, vol. 2, no. 4, pp. 859–869, Dec. 2014.
[33] S. Qin, S. T. Cady, A. D. Dominguez-Garcia, and R. C. N. Pilawa-Podgurski, "A distributed approach to maximum power point tracking for photovoltaic submodule differential power processing," *IEEE Trans. Power Electron.*, vol. 30, no. 4, pp. 2024–2040, Apr. 2015.
[34] Linear Technology LTC3300-1 Datasheet. (2016). [Online]. Available: http://cds.linear.com/docs/en/datasheet/33001fb.pdf
[35] S. Poshtkouhi, A. Biswas, and O. Trescases, "DC-DC converter for high granularity, sub-string MPPT in photovoltaic applications using a virtual-parallel connection," in *Proc. 2012 27th Annu. IEEE Appl. Power Electron. Conf. Expo.*, Feb. 2012, pp. 86–92.
[36] T. Shimizu, M. Hirakata, T. Kamezawa, and H. Watanabe, "Generation control circuit for photovoltaic modules," *IEEE Trans. Power Electron.*, vol. 16, no. 3, pp. 293–300, May 2001.
[37] U. Tröltzsch and O. Kanoun, "Miniaturized impedance measurement system for battery diagnosis," in *Proc. SENSOR 2009*, 2009, vol. I, pp. 251–256.
[38] C. Olalla and D. Clement, "Architectures and control of submodule integrated dc–dc converters for photovoltaic applications," *IEEE Trans. Power Electron.*, vol. 28, no. 6, pp. 2980–2997, Jun. 2013.
[39] J. T. Stauth, M. D. Seeman, and K. Kesarwani, "A resonant switched-capacitor IC and embedded system for sub-module photovoltaic power management," *IEEE J. Solid-State Circuits*, vol. 47, no. 12, pp. 3043–3054, Dec. 2012.
[40] S. E. Li, B. Wang, H. Peng, and X. Hu, "An electrochemistry-based impedance model for lithium-ion batteries," *J. Power Sources*, vol. 258, pp. 9–18, 2014.
[41] U. Tröltzsch, O. Kanoun, and H.-R. Tränkler, "Characterizing aging effects of lithium ion batteries by impedance spectroscopy," *Electrochim. Acta*, vol. 51, pp. 1664–1672, 2006.

Eric Din received the A.B. and M.S. degrees in engineering sciences from Thayer School of Engineering, Dartmouth College, Hanover, NH, USA, in 2014 and 2016, respectively.

He is co-founding Hive Battery, where he is researching novel battery diagnostic technologies.

Christopher Schaef (S'11) received the B.S. and M.S. degrees in industrial engineering from Helmut-Schmidt University, Hamburg, Germany, in 2010 and 2011, respectively, and the Ph.D. degree from Dartmouth College, Hanover, NH, USA, in 2016.

He is currently a Power Delivery Researcher in the Circuits Research Laboratory, Intel Corporation, Santa Clara, CA, USA. His research interests include IC design, energy harvesting, and high-density dc–dc converters.

Keith Moffat (S'16) received the B.E. and A.B. degrees in engineering sciences from Thayer School of Engineering, Dartmouth College, Hanover, NH, USA, in 2016. He is currently working toward the Ph.D. degree at the University of California, Berkeley, CA, USA, where he is working on renewable energy integration, control, and optimization.

Jason T. Stauth (M'99) received the M.S. and Ph.D. degrees from the University of California, Berkeley, CA, USA, in 2006 and 2008, respectively, where he studied high-frequency power electronics and radio-frequency power amplifiers.

He has been an Assistant Professor at Dartmouth College, Hanover, NH, USA, since 2011. His research interests include high-density power electronics and integrated circuits for applications in renewable energy, transportation, and energy storage.

Prof. Stauth received the National Science Foundation Career Award in 2016.